Toward Intrinsic Force Sensing and Control in Parallel Soft Robots

Lukas Lindenroth , *Member, IEEE*, Danail Stoyanov , *Senior Member, IEEE*, Kawal Rhode, and Hongbin Liu

Abstract—With soft robotics being increasingly employed in settings demanding high and controlled contact forces, recent research has demonstrated the use of soft robots to estimate or intrinsically sense forces without requiring external sensing mechanisms. While this has mainly been shown in tendon-based continuum manipulators or deformable robots comprising of push–pull rod actuation, fluid drives still pose great challenges due to high actuation variability and nonlinear mechanical system responses. In this work, we investigate the capabilities of a hydraulic, parallel soft robot to intrinsically sense and subsequently control contact forces. A comprehensive algorithm is derived for static, quasi-static, and dynamic force sensing, which relies on fluid volume and pressure information of the system. The algorithm is validated for a single degree-of-freedom soft fluidic actuator. Results indicate that axial forces acting on a single actuator can be estimated with mean error of 0.56 ± 0.66 N within the validated range of 0–6 N in a quasi-static configuration. The force sensing methodology is applied to force control in a single actuator as well as the coupled parallel robot. It can be seen that forces are controllable for both systems, with the capability of controlling directional contact forces in case of the multidegree-of-freedom parallel soft robot.

Lukas Lindenroth was with the Wellcome/EPSRC Centre for Interventional and Surgical Sciences (WEISS), University College London, London W1W 7EJ, U.K. He is now with the Department of Surgical & Interventional Engineering, School of Biomedical Engineering and Imaging Sciences, King's College London, London WC2R 2LS, U.K. (e-mail: lukas.lindenroth@kcl.ac.uk).

Danail Stoyanov is with the Wellcome/EPSRC Centre for Interventional and Surgical Sciences (WEISS), University College London, London W1W 7EJ, U.K. (e-mail: danail.stoyanov@ucl.ac.uk).

Kawal Rhode is with the School of Biomedical Engineering and Imaging Sciences, King's College London, London WC2R 2LS, U.K. (e-mail: kawal.rhode@kcl.ac.uk).

Hongbin Liu is with the Institute of Automation, Chinese Academy of Sciences, and Centre of AI and Robotics (CAIR), Hong Kong Institute of Science & Innovation, Chinese Academy of Sciences, Beijing 100045, China, and also with the School of Biomedical Engineering and Imaging Sciences, King's College London, London WC2R 2LS, U.K. (e-mail: hongbin.liu@kcl.ac.uk).

Index Terms—Force control, force feedback, hydraulic actuators, soft robotics.

I. INTRODUCTION

SOFT robots have gained popularity following the paradigm shift in automation away from deterministic factory settings to collaborative, human-in-the-loop use-cases, and medical procedures [1]. Due to their compliance and softness when brought into contact with the environment, soft robots are inherently safer given that high contact forces are mitigated through deformation around the point of contact. While there are a number of application scenarios in which high compliance of the robot is of paramount importance, significant deformability limits the usage of such robots for tasks requiring accurate positioning or precise loadbearing, as for example seen in catheter robotic systems [2] or soft robot grippers [3].

If the envisioned application requires contact with a target or load bearing, a soft robot can be designed such that it is capable of exerting forces in a specific direction, while retaining high degrees of compliance in others, which consequently leads to highly underactuated systems. In our previous work, we have shown that this approach is particularly viable in medical applications, such as ultrasound imaging, and a parallel soft robotic system has been proposed, which exhibits significant compliance in some DOFs while remaining stiff in others [4]. The system is designed around spring-reinforced soft fluidic actuators (SFAs) [5] as shown in Fig. 1(a). The soft robotic end-effector (SEE) system is capable of applying loads commonly found in ultrasound imaging without exhibiting substantial deformation in the contact force direction. While the system has been proposed with the application of medical ultrasound in mind, such a soft parallel mechanism is highly adaptable and could be employed for a wide range of applications requiring the adaptability of a soft robot with the ability to control contact forces. An overview of the system equipped with an ultrasound probe is shown in Fig. 1(b). Such high force and high stiffness soft robotics systems can, in contrast to their highly compliant counterparts, pose risks to their environments and, in case of medical robotic systems, patients. Sensing applied forces becomes therefore crucial for safe usage of such robots. To keep system complexity minimal, integrated mechanisms for sensing and controlling applied contact forces have to be derived.

In current soft robotic systems force sensing are predominantly achieved by attaching dedicated force–torque sensors at
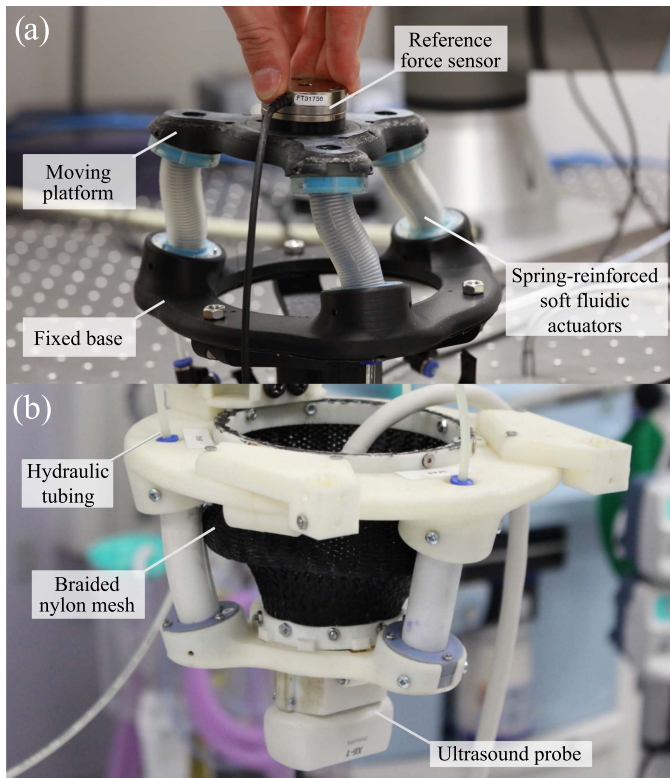
Fig. 1. Soft robotic end-effector driven by extensible soft fluidic actuators (SFAs) under external loading (a) and example application of the system for extracorporeal ultrasound (b).

the desired contact point on the robot's body or in close proximity to it. For this purpose, rigid, miniature force sensors have been developed and efficiently applied for example in medical procedures, minimally invasive surgery, and others. Different approaches have been developed based on physical quantities such as displacement and strain, resistance, or pressure. An extensive review is given in [6]. Tip force sensors are particularly employed in continuum systems [7]. For the purpose of creating custom sensors, fibre optics show due to their flexible nature good applicability to measuring strains in sensing structures. Various fibre optics-based force sensors have been presented in [8] and [9]. A larger scale body contact sensor has been applied to a soft surgical manipulator in [10]. It has been proposed to employ a rigid force sensor at the base of a soft robotic manipulator, thus maintaining a soft interaction [11]. The accuracy of estimating the force applied at a defined contact point along the robot's body is then highly dependent on the employed model as well as the feedback methodology for providing strain or deformation measures. Moreover, is the location of contact unknown or multiple forces act along the robot's body the approach fails.

Advances in material sciences have resulted in the development of flexible sensors, which show the potential to be integrated in the elastomeric bodies of soft robots. Such sensors make use of e.g., piezoelectric polymers [12] or fluidic channels filled with liquid metal [13]. An overview on recent soft electronics sensors is given in [14].

While the abovementioned concepts employ dedicated sensing devices attached to or embedded in the soft robotic structure, the robot could itself, due to its deformable and adaptive nature, be utilized to determine externally applied forces. This is commonly referred to as *force estimation*. It has been shown that the information contained in the shape of the robot can be used to approximate the applied loading [15]. Rucker and Webster [16] presented a probabilistic approach to force sensing in a continuum robot. A shape reconstruction algorithm with consecutive statics model is proposed in [17]. A feature-based visual tracking algorithm combined with a finite element model for estimating external forces is presented in [18]. These approaches, however, require at least partial or in some cases full knowledge about the deformed shape of the manipulator, which is often limited either by the field of view or the update rate of the given sensing modalities. In [19], the external tip force acting on a steerable catheter robot has been investigated using electromagnetic marker tracking, indicating good applicability to clinical applications in which EM trackers are commonly used for catheter guidance.

Other investigations have shown that, besides the shape, the feedback in the actuator space of the robot could be utilized to determine externally applied forces, which is commonly referred to as *intrinsic force sensing*. Sensing external forces intrinsically offer a number of inherent advantages. Dedicated force–torque sensors can be omitted from the design and sensors while sensors employed for intrinsic sensing can be positioned away from the end-effector, which can lead to simplified designs and entirely compliant interfaces between end-effector and environment. Extensive work has been conducted in intrinsically sensing the tip wrenches in multisegment continuum robots [20], [21]. In [22], Haraguchi et al. proposed a disturbance observer approach to determine external forces applied to a pneumatic manipulator, which is limited by the backbone material of the flexible joint required for the force sensing approach. Black et al. [23] presented an actuator space-based force sensing approach for a parallel continuum robot. In our previous work, we have shown that external forces applied to a hydraulic soft robotic manipulator can be related to internal hydraulic pressure variations in the actuating fluid given that an accurate model of the manipulator shape exists [24].

In this article, we derive an intrinsic force controller, which relies entirely on measurements of actuation pressures and induced fluid volumes. This is achieved by describing the intrinsic force sensing in the actuator space of the system and translating it into Cartesian space. Force sensing and control are derived for independent, single degree of freedom (DOF) soft fluidic actuators (SFAs) initially and combined for describing force control in a 3DOF parallel soft robotic end-effector (SEE), which is validated in clamping contacts. In summary, this work contributes the following:

1) Analysis of the internal pressure characteristics of an SFA under inflation and external loading, which enables distinction between internal pressures caused by the SFA material strain and loads applied to the tip of the SFA.
2) Force estimation in an SFA, which enables the intrinsic sensing of external forces under varying internal fluid volumes.
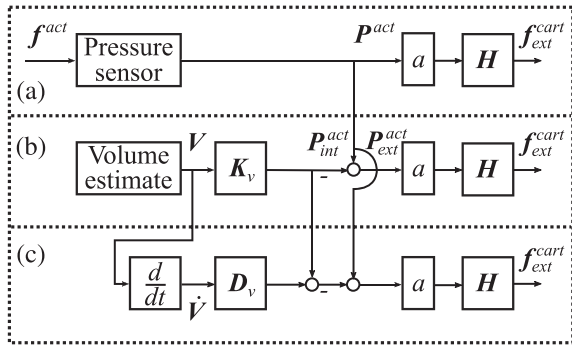
Fig. 2. Overview of *static* (a), *quasi-static* (b), and *dynamic* intrinsic force sensing algorithms (c).

Fig. 3. Free-body diagram of an SFA in deflated and inflated configurations under internal loading due to extension f_{int}^{act} and external loading f_{ext}^{act}.

3) A novel intrinsic force controller, which relies solely on fluidic pressure and the known kinematic constraints applied to the system to sense and regulate external forces in a dynamic environment.

4) Validation of the intrinsic force controller with a single SFA and the combined SEE with a stationary clamping contact under varying loads and inflation levels.

II. METHODOLOGIES

Intrinsic force sensing in extensible soft robots is highly dependent on the robots' states and loading conditions. In the following, it is elaborated how static intrinsic sensing can be achieved when the robot configuration is ignored, which is demonstrated given the example of a single SFA. A lumped modeling approach is then described to consider configuration changes in the SFA. An approach to quasi-static and dynamic intrinsic force sensing is derived and force controllers are proposed for a single SFA and the SEE.

To simplify the derived control approach, force sensing and control are derived in the actuator space of the system. Forces are then related to the Cartesian space. Vectors containing forces and moments or kinematic information are denoted as $*^{act}$ and $*^{cart}$ when represented in actuator or Cartesian space, respectively. An overview of the algorithms for *static*, *quasi-static*, and *dynamic* intrinsic force sensing is provided in Fig. 2.

A. Static Force Sensing

In static force sensing, the configuration-dependency of the internal fluid pressure is ignored. Here, the robot is positioned in a given configuration and external forces are directly related to the pressure variation in the actuator space of the system. An external force applied along the direction of extension of the SFA induces a hydraulic pressure change of the form

$$f_{ext}^{act} = P_{ext}^{act} \cdot a \tag{1}$$

where f_{ext}^{act} is the component of the external force acting along the direction of actuation of the SFA, P_{ext}^{act} the resultant hydraulic pressure and a the cross-sectional area of fluid channel.

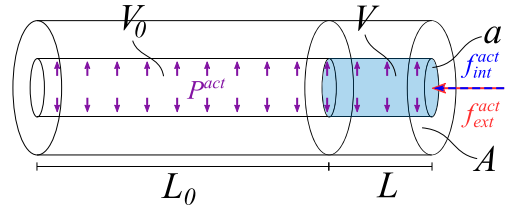This formulation can be expanded to a parallel assembly of multiple SFAs by determining the wrench transformation between a rigidly connected frame and the individual SFAs, as it has been shown in our previous work for the previously derived SEE [5]. Assuming a known, rigid transformation between actuators and a desired reference frame H, the relationship can be written as

$$f_{ext}^{cart} = H \cdot P_{ext}^{act} \cdot a \tag{2}$$

where $f_{ext}^{cart} \in [3 \times 1]$ is the external force applied in Cartesian space, a the cross-sectional area of the actuator fluid chamber and $P_{ext}^{act} \in [n \times 1]$ the vector of external pressure applied to the n individual actuators. H transforms the external force from actuator space into Cartesian space, such that

$$H = \begin{bmatrix} \partial f_x^{cart}/\partial f_1^{act} & \partial f_x^{cart}/\partial f_2^{act} & \ldots & \partial f_x^{cart}/\partial f_n^{act} \\ \partial f_y^{cart}/\partial f_1^{act} & \partial f_y^{cart}/\partial f_2^{act} & \ldots & \partial f_y^{cart}/\partial f_n^{act} \\ \partial f_z^{cart}/\partial f_1^{act} & \partial f_z^{cart}/\partial f_2^{act} & \ldots & \partial f_z^{cart}/\partial f_n^{act} \end{bmatrix} \tag{3}$$

where n is the number of actuators in the system. The formulation also holds for moments applied to the parallel structure, which will be ignored in this work given the limited number of SFAs employed in the SEE.

While in an kinematically constrained extensible actuator a can be considered as constant, in reality the cross-sectional area of the fluid chamber changes under increasing fluid volume. Moreover, if the hydraulic fluid system contains entrapped air, the mechanical transmission between external force and hydraulic pressure change might be nonconstant. Therefore, in practice, a can be considered as the force transmission of the system and has to be approximated and experimentally determined.

B. Quasi-Static and Dynamic Force Sensing

Variation in the internal fluid volume V leading to strain in the actuator induces stress, which is reflected in form a hydraulic pressure P_{int}. Hence, changes in fluid volume within the actuators, and as such in the state of the system, need to be considered when estimating external forces.

The internal stress σ exerted by an elastic body under an induced strain ϵ can be described

$$\sigma = E \cdot \epsilon \tag{4}$$

where E is the Young's Modulus of the elastic material. For a linear, isotropic elastic cylinder with an internal cavity of cross-sectional area a as shown in Fig. 3, a linearized local extension can be expressed as a function of the internal force f_{int}^{act}, such
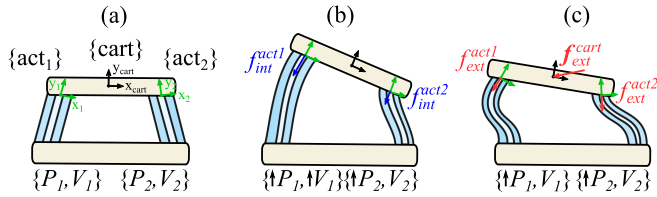
Fig. 4. Configurations of the deflated SEE (a), under internal fluid volume variation, leading to internal reaction forces $f_{\text{int}}^{\text{act}_i}$ (b) and under internal and external forces $\boldsymbol{f}_{\text{ext}}^{\text{cart}}$ (c).

that

$$f_{\text{int}}^{\text{act}} = \frac{EA}{L_0}L = \frac{EA}{aL_0}V \tag{5}$$

where L_0 and V_0 are the initial length and fluid volume of the actuator and L and V the respective increments in SFA extension and introduced fluid volume, respectively. A is the total cross-sectional area of the SFA without the cross-sectional area of the fluid channel, which is denoted as a. An overview of the variables is indicated in Fig. 3. The resultant internal pressure can be written as

$$P_{\text{int}}^{\text{act}} = \frac{EA}{a^2 L_0}V = K_V V \tag{6}$$

where K_V is the stiffness of the SFA.

If an external force is applied to the system along the direction of actuation then, under static equilibrium conditions, the following holds for the total hydraulic pressure P^{act} in the system

$$P^{\text{act}} = P_{\text{int}}^{\text{act}} + P_{\text{ext}}^{\text{act}} \tag{7}$$

where the total hydraulic pressure in the actuator is measurable by introducing a pressure transducer to the fluid system. To infer the external force applied axially to the SFA, one can employ the derived model such that

$$P_{\text{ext}}^{\text{act}} = P^{\text{act}} - P_{\text{int}}^{\text{act}} = P^{\text{act}} - K_V V. \tag{8}$$

In case of the SEE, actuators are coupled in parallel. Thus, volume variation in a single SFA not only affects its internal pressure $P_{\text{int}}^{\text{act}}$, but the internal pressures and resulting forces of all coupled SFAs $\boldsymbol{f}_{\text{int}}^{\text{act}}$. Force variations $f_i^{\text{act}} = f_{\text{int},i}^{\text{act}} + f_{\text{ext},i}^{\text{act}}$ act in the local frame of the respective ith SFA $\{\text{act}_i\}$, as shown in Fig. 4.

Expressing the stiffness for the combined mechanism therefore yields

$$\boldsymbol{K}_V = \begin{bmatrix} k_{11} & k_{12} & k_{13} \\ k_{21} & k_{22} & k_{23} \\ k_{31} & k_{32} & k_{33} \end{bmatrix} \tag{9}$$

where k_{ii} are the independent SFA stiffnesses and k_{ij} the effects induced by volume variations of coupled SFAs. While an analytical formulation can be found following the derivations shown in our previous work [5], the elements of $\boldsymbol{K}_V$ not only depend on the elastic properties of the SFAs, but on the combined stiffness of actuators and fluidic drive system. The latter can be greatly affected by the chosen tubing and entrapped air among other factors. Therefore, in practice, $\boldsymbol{K}_V$ should be calibrated prior to sensing external forces.

The linear stiffness of the SFAs can be estimated by determining the pressure response of the system when inducing known fluid volumes $\boldsymbol{V} = [V_1, V_2, \ldots, V_n]^T$ with n indicating the number of independent actuators. For a single DOF system, this can be achieved by inducing and retracting volume across the extension range of the actuator and linearizing the pressure response. For the multi-DOF system, samples have to be acquired across the actuator space to consider configurations in which coupling forces occur between the actuators. The stiffness can then be estimated by solving the linear least-squares problem

$$\underset{\hat{\boldsymbol{K}}_V}{\text{minimise}} \quad ||\hat{\boldsymbol{K}}_V \boldsymbol{V} - \boldsymbol{P}_{\text{int}}^{\text{act}}|| \tag{10}$$

where $\hat{\boldsymbol{K}}_V$ is the approximated stiffness in the actuator space of the system

This can then be related to the external force in Cartesian space by

$$\boldsymbol{f}_{\text{ext}}^{\text{cart}} = \boldsymbol{H}(\boldsymbol{P}^{\text{act}} - \boldsymbol{K}_V \boldsymbol{V}) \cdot a. \tag{11}$$

For fast SFA extensions, the damping of the system due to long fluidic lines becomes significant. Assuming linear damping with the damping coefficient D_V, the internal force of the actuator can then be expressed as

$$P_{\text{int}}^{\text{act}} = K_V V + D_V \dot{V} \tag{12}$$

where $\dot{V}$ expresses the actuation fluid flow rate.

For the combined SEE, the external force under consideration of damping caused by the fluid flow becomes

$$\boldsymbol{f}_{\text{ext}}^{\text{cart}} = \boldsymbol{H}(\boldsymbol{P}^{\text{act}} - \boldsymbol{K}_V \boldsymbol{V} - \boldsymbol{D}_V \dot{\boldsymbol{V}}) \cdot a. \tag{13}$$

Alike the stiffness of the system, $\boldsymbol{D}_V$ is determined experimentally. This is achieved by introducing working fluid at a defined flowrate and measuring the damping-induced pressure response. The damping coefficient is then linearized for each SFA.

C. Force Control

Based on the previously derived characteristics of the system, a linear force controller can be defined to drive the contact force to a desired force setpoint $\boldsymbol{f}_d^{\text{cart}}$ in Cartesian space.

For a single SFA, a generic force PID controller can be defined as

$$\dot{V}_d = G_P f_e^{\text{act}} + G_I \int_t f_e^{\text{act}} dt + G_D \dot{f}_e^{\text{act}} \tag{14}$$

where G_P, G_I, and G_D are the proportional, integral, and derivative gains, respectively. $\dot{V}_d$ is the demanded SFA flow rate and f_e^{act} denotes the force error in actuator space such that

$$f_e^{\text{act}} = f_d^{\text{act}} - f_{\text{ext}}^{\text{act}}.$$

With the demanded force f_d^{act} along the central channel of the SFA. For the multi-DOF system with an arbitrary force direction in Cartesian space the force control law becomes

$$\dot{\boldsymbol{V}}_d = \boldsymbol{G}_P \boldsymbol{f}_e + \boldsymbol{G}_I \int_t \boldsymbol{f}_e dt + \boldsymbol{G}_D \dot{\boldsymbol{f}}_e \tag{15}$$

where $\boldsymbol{G}_P$, $\boldsymbol{G}_I$, and $\boldsymbol{G}_D$ are diagonal gain matrices. The force error can then be defined in actuator space by

$$\boldsymbol{f}_e = \boldsymbol{f}_d^{\text{act}} - \boldsymbol{f}_{\text{ext}}^{\text{act}} = \boldsymbol{H}^{-1}\boldsymbol{f}_d^{\text{cart}} - \boldsymbol{P}_{\text{ext}}^{\text{act}} \cdot a \quad (16)$$

with the demanded force in Cartesian space $\boldsymbol{f}_d^{\text{cart}} = [f_{d,x}, f_{d,y}, f_{d,z}]^T$.

D. Experimental Validation

Experimental setups are created to validate the accuracy of the proposed intrinsic sensing and control approaches for the soft robotic ultrasound end-effector, which has been presented in our previous work and is shown in Fig. 1 [5]. It is comprised of three SFAs arranged in parallel, linking the moving top platform to a fixed base. Unless stated otherwise, the SFAs are fabricated from two types of silicone rubber, namely Dragon Skin 10NV for the SFA body and Smooth-Sil 960 for the endcaps (Smooth-On Inc., Pennsylvania, USA), and comprise of a central channel which is spring-reinforced. The system is moreover equipped with a braided nylon mesh, which has been shown to eliminate twist between the two platforms, thus, greatly improving load-bearing capabilities when an external wrench is applied. The inflation level of the actuators, which corresponds to the percentage of introduced fluid volume relative to the maximum volume of 5 ml, is regulated by three stepper motor-driven syringe pumps. Assuming negligible compressibility of the working fluid, the linear syringe pump system allows for efficient estimation of the introduced fluid volumes from the syringe plunger position and hence the rotational angle of the stepper motors. Fluid pressures are monitored by dedicated analogue pressure sensors (Shenzhen Yibai Network Technology Co., Ltd., China), which are introduced into the fluid channels.

To determine the effect of the SFA state and shape on the force transmission of the system, it is characterized by applying compression loads acting along the main axis of the SFA and measuring the resulting hydraulic pressure variation. For this purpose, the base of the SFA is fixed and its tip is slowly displaced by 2 mm perpendicular to the SFA tip's surface using a robot manipulator (UR3, Universal Robots, Odense, Denmark). The resulting force applied to the SFA is measured with a force–torque sensor (Gamma, ATI, Apex, USA). An overview of the setup is provided in Fig. 5(a). The measurement is repeated for different levels of extension in 0.5 ml volume and 10 deg bending increments. Bending poses are obtained assuming a constant curvature arc given the length of the SFA and a desired tip bending angle. The force transmission is characterized for varying inflation volumes V and bending angles θ.

To verify the pressure and extension behavior of an SFA with a minimal influence of bending and shearing, a railed experimental setup is constructed. It comprises of two linear guides to which the SFA tip is connected. Two stainless steel rods are attached to an aluminium profile through two 3d-printed bracket elements. A sliding element is added, which contains one linear bearing (LM6UU) per guide to reduce friction. The slider is connected to a linear potentiometer (100 mm stroke length), which is fixed to the aluminium profile. The SFA is fixed to one of the bracket elements and attached to the slider.
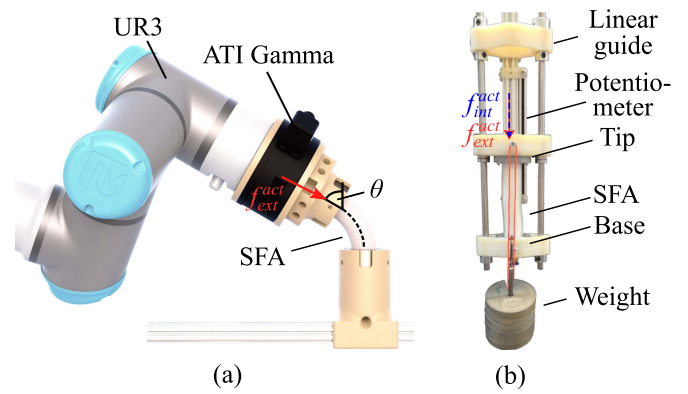

Fig. 5. Experimental setups for SFA loading characterisation. The SFA tip is displaced by a robot manipulator (UR3) under a given bending angle θ and the resulting force $f_{\text{ext}}^{\text{act}}$ measured by an inline force–torque sensor (ATI Gamma) (a). Weights are applied to the tip of the linearly guided SFA to determine loading for different extensions (b).
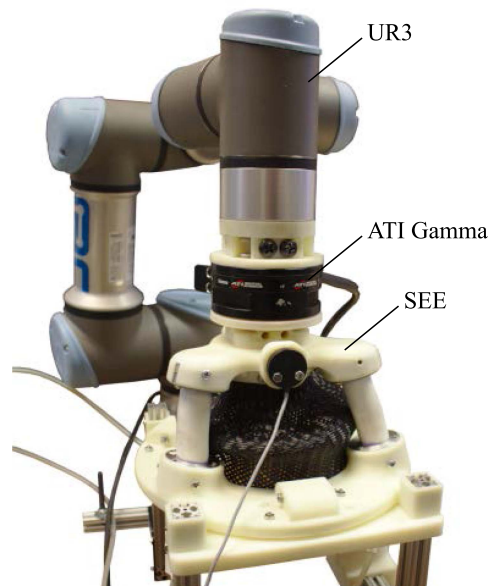

Fig. 6. Experimental setup for force control evaluation with clamping contact provided by a robotic manipulator.

Upon inflation, the slider is moved and a proportional voltage is measurable across the potentiometer. The pressure inside the hydraulic tubing is measured using a capacitive pressure transducer. A depiction of the experimental setup is presented in Fig. 5(b).

The force controller for a single SFA as well as the integrated SEE are validated under a clamping contact constraint, which is achieved by affixing the base of the SFA and SEE and attaching the tip via a force–torque sensor to a robotic manipulator. Exemplary setups are shown for the single SFA in Fig. 5(a) and for the SEE in Fig. 6. The individual SFAs are actuated through linear syringe pumps, as introduced in our previous work [5]. The controller is executed at a frequency of 250 Hz and pressure data is filtered using an exponential moving average filter with a cutoff frequency of 100 Hz.
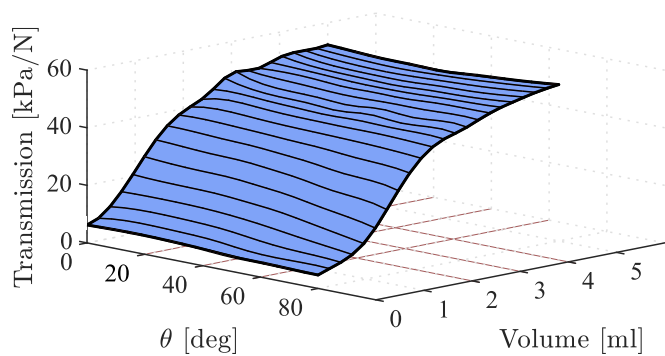
Fig. 7. Force transmission of a single SFA with inflation and bending.

III. RESULTS

A. Static Force Sensing

The force transmission as a function of the SFA inflation volume V and bending angle θ is presented in Fig. 7. It follows a highly nonlinear trend with the induced working fluid volume, which approaches a constant value for volumes greater than 2.5 ml. The effect of bending, however, is negligible compared to the sensitivity change due to extension. To simplify the dynamic control of the system, in the following, the SFA will only be controlled in a region with minimal change to the transmission, which is achieved by limiting inflation volumes to ≥ 2.5 ml. For this range, the force transmission is 48.5 ± 3.25 kPa/N. The error introduced by linearizing the force transmission of the SFA is therefore 6.69% of the maximum inflation pressure. The error introduced by bending the actuator is insignificant compared the change in inflation and is therefore ignored.

The obtained force transmissibility is applied to verify the static and quasi-static force sensing capabilities of the SFA. In the static force sensing experiment, internal pressure $P_{\text{int}}^{\text{act}}$ is sensed once a desired inflation is reached and thus, pressure effects induced by the fluid volume are ignored. In quasi-static force sensing the internal pressure is estimated as a function of the induced fluid volume.

The SFA is attached to a linear guide and for different levels of extension, loads in form of weights are applied axially through a cable. Given the previously derived constant force transmission, the applied forces are estimated as indicated in (1).

The SFA is inflated in a range from 50% to 100% in 10% increments. For each inflation state, weights inducing loads of 2 N, 4 N, and 6 N are incrementally added to the tendon attached to the tip of the SFA before a new inflation volume is approached. The results are shown in Fig. 8, where Fig. 8(a) shows the force error averaged over the applied loads for varying inflation and Fig. 8(b) the force error averaged over the different inflation levels for varying force levels.

The results indicate that the inflation level has a less significant effect on the force sensing accuracy as the force level in static force sensing. While the force error remains almost constant throughout different levels of inflation at 0.15 ± 0.18 N, the error due to the applied load increases from 0.18 ± 0.11 N for a load of 2 N to 0.26 ± 0.36 N at 6 N. It can be concluded that, without
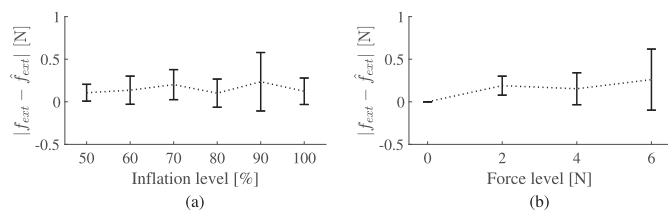

Fig. 8. Force error in static intrinsic force sensing for different inflations (a) and loads (b) of a single SFA.
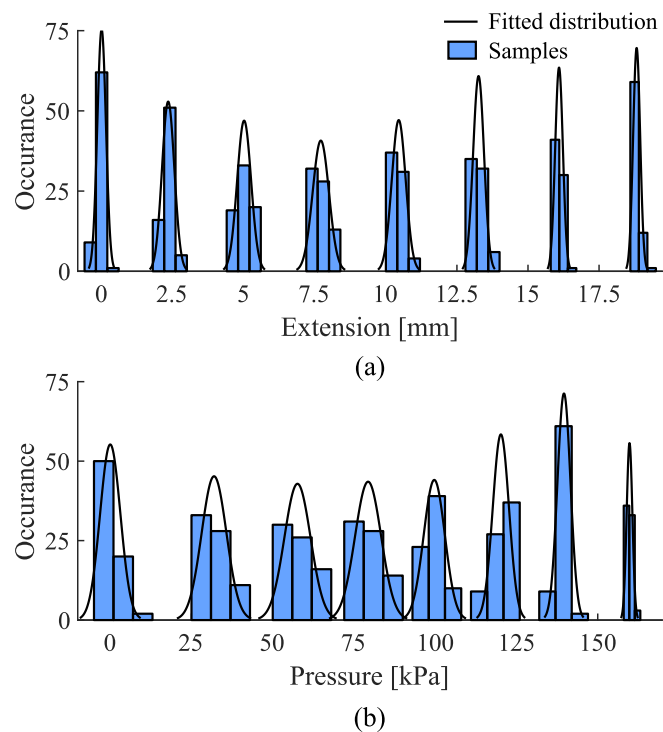

Fig. 9. Variation in SFA extension (a) and pressure (b) for repeated volume variations across 500 repetitions.

the contribution of uncertainty from randomised movements of the SFA, higher forces applied to the SFA lead to less accurate force sensing, while the inflation of the SFA does not contribute significantly to a change in error.

B. Quasi-Static Force Sensing

To demonstrate the effect caused by other unconsidered mechanical phenomena and to establish a maximum accuracy with which the internal pressure inside the SFA and thus the state of the SFA can be estimated as a function of the induced fluid volume, a repeatability experiment is conducted. To this end, a set amounts of working fluid are induced into the SFA and the extension and pressure responses are recorded in steady state. To ensure consistency of the results, this is repeated 500 times. The order of the demanded volumes is randomized to show the effect of history-dependent phenomena such as hysteresis.

Results of the experimental validation are shown in Fig. 9. The standard deviations for each SFA state are presented in

TABLE I
STATE ESTIMATION ACCURACY

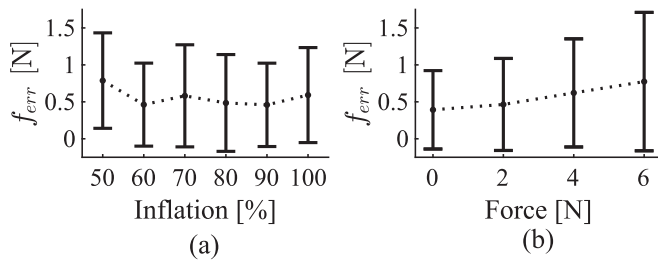| Volume [%]	$\sigma(x)$[mm]	$\sigma(P)$[kPa]
0	0.15	3.12
14.29	0.22	3.81
28.57	0.25	4.02
42.90	0.29	4.01
57.14	0.24	3.30
71.43	0.19	2.49
85.71	0.14	2.01
100.0	0.12	0.88
μ	0.20	2.95

Fig. 10. Force error in quasi-static intrinsic force sensing for varying inflation (a) and force levels (b) of a single SFA

Table I. The accuracy in both the SFA length and pressure vary substantially with the induced extension. It is worth noting that due to the nonlinear relationship between extension and pressure for a given fluid volume inside the SFA the mean extension and pressure values resulting from eight volume setpoints are not equally spaced. While the positioning uncertainty reaches local minima of 0.15 and 0.12 mm at the 0% and 100% of volume, a maximum standard deviation 0.29 mm is observed at 42.9% extension. A similar trend is observable in the pressure sensing. The pressure sensing uncertainty reaches its minimum at 100% extension and a maximum of 4.02 kPa at 28.57% extension. The mean SFA state uncertainty is 0.2 mm in position and 2.95 kPa in pressure. Taking into account the force transmissibility of the system, this relates to an uncertainty in force of 0.06 N.

An experimental validation of the quasi-static force sensing capabilities of the SFA is conducted. A randomised sequence of 100 poses in the range from 50 to 100% extension with increments of 10% is generated. A random load of 0 N, 2 N, 4 N, or 6 N is assigned to each pose and attached to the SFA once the pose target is reached and dynamic pressure variations have settled. The resulting data are summarized for varying inflation level in Fig. 10(a) and for varying force level in Fig. 10(b).

In comparison to the results of the static force sensing experiment, the mean error across all configurations is increased from 0.15±0.18 N to 0.56±0.66 N. Similar to the previous results, it can be seen that the accuracy of the estimation decreases with the applied load, from 0.39±0.53 N at 0 N load to 0.77±0.94 N at 6 N. While the accuracy decreases with the applied load, it is only minimally affected by the inflation level. The external force applied to the SFA can be estimated with an average accuracy of 0.56 N±0.66 N across all configurations.
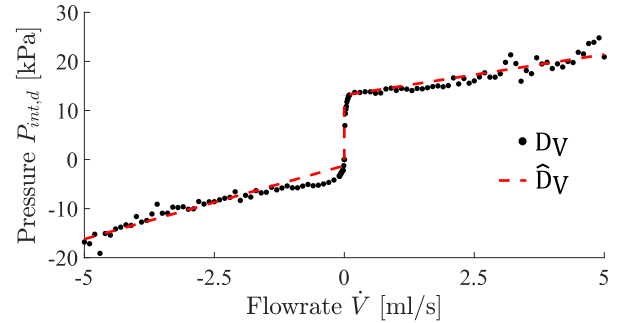

Fig. 11. Damping pressure for different flow rates $\dot{V}$ of a single SFA.

To be able to compensate for pressure variation due to high fluid flow rates, an experiment is conducted to determine the pressure drop associated with a given flow rate. The SFA is attached to the linear guide and inflated with a known flow rate. Upon reaching its maximum inflation, it is deflated with the same flow rate. Flow rates are varied between 0 and 5 ml/s, and the resultant damping coefficient D_V computed such that

$$D_V = \frac{P - K_V V}{\dot{V}}. \tag{17}$$

50% of the beginning of each trajectory is ignored due to pressure fluctuations induced by the rapid acceleration of the system. The results of the evaluation are presented in Fig. 11, where each sample corresponds to the computed damping pressure $P_{int,d} = D_V \dot{V}$ for a given constant flow rate of the SFA across one inflation and deflation cycle. The pressure offset caused by the damping of the system is highly discontinuous and nonlinear. It can be described by a discontinuous function of the form

$$\hat{D}_V = \begin{cases} 3.00\frac{kPa}{ml/s} \cdot \dot{V} - 16.82\,kPa, & \dot{V} \leq 0\,ml/s \\ 13.1\,kPa, & 0\,ml/s < \dot{V} \leq 0.1\,ml/s \\ 1.66\frac{kPa}{ml/s} \cdot \dot{V} + 13.10\,kPa, & 0.1\,ml/s < \dot{V} \end{cases} \tag{18}$$

To simplify the controller and avoid discontinuities, the combined damping as a function of the flow rate is linearized across the investigated flowrate ranges. For the given SFA, the linearized damping is determined as $4.46\frac{kPa}{ml/s}$.

C. SFA Force Control

To verify the performance of the force controller, step responses of the system are recorded for steps with demand forces of 0 N, 2 N, 4 N, and 6 N of axial force. For that purpose the base and tip are fixed in space before the step is demanded. Due to the possible variability of the force controller performance with the extension length of the SFA, data are recorded for initial inflation volumes V_{init} of 50%, 60%, 70%, and 80%. For the single SFA, a *PD*-controller with $G_P = 1.97\frac{ml}{s \cdot N}$ and $G_D = 0.2\frac{ml}{s^2 \cdot N}$. Upon reaching the demanded force, the SFA is deflated, inflated to V_{init} and the next target force is approached.

This article has been accepted for inclusion in a future issue of this journal. Content is final as presented, with the exception of pagination.

8   IEEE/ASME TRANSACTIONS ON MECHATRONICS
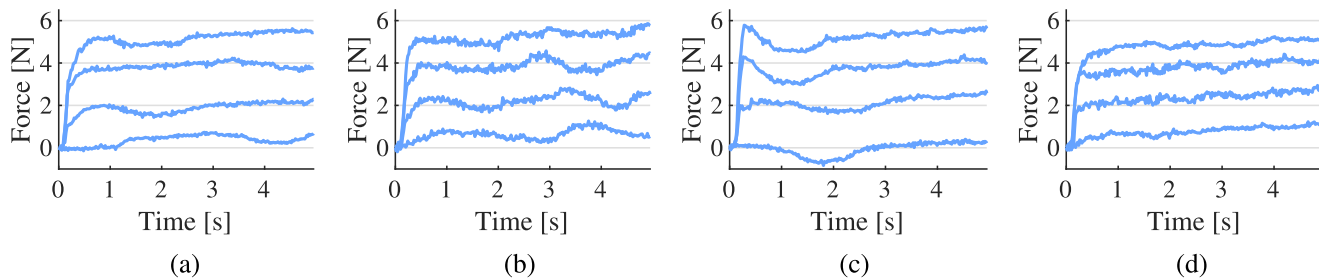

Fig. 12.   Results for SFA step responses at 50% (a), 60% (b), 70% (c), and 80% (d) initial inflation showing the measured forces for varying force demands of 0 N, 2 N, 4 N, and 6 N.

TABLE II
STEADY STATE ERROR OF THE SFA FORCE CONTROLLER FOR VARYING INFLATION LEVELS AND TARGET FORCES

V_{init} \ f_d^{act}	0N	2N	4N	6N	μ
50%	0.48N	0.20N	0.13N	0.74N	0.39N
60%	0.67N	0.36N	0.26N	0.59N	0.47N
70%	0.27N	0.35N	0.18N	0.61N	0.35N
80%	0.93N	0.55N	0.18N	1.02N	0.67N
μ	0.59N	0.36N	0.19N	0.74N	0.47N

TABLE III
SEE FORCE CONTROL STEADY STATE ERROR FOR DIFFERENT INFLATION LEVELS AND TARGET FORCES IN x-DIRECTION

V_{init} \ $f_{d,x}^{\text{cart}}$	-5N	-2.5N	0N	2.5N	5N	μ
50%	1.66±0.63N	0.98±0.56N	0.47±0.55N	0.55±0.48N	1.56±0.56N	1.04±0.55N
60%	1.52±0.37N	0.94±0.35N	0.36±0.44N	0.84±0.55N	1.12±0.62N	0.96±0.42N
70%	1.53±0.36N	0.89±0.33N	0.31±0.35N	0.65±0.48N	1.11±0.55N	0.90±0.46N
80%	1.56±0.36N	0.57±0.43N	0.39±0.48N	0.72±0.26N	0.73±0.43N	0.79±0.45N

TABLE IV
SEE FORCE CONTROL STEADY STATE ERROR FOR DIFFERENT INFLATION LEVELS AND TARGET FORCES IN y-DIRECTION

V_{init} \ $f_{d,y}^{\text{cart}}$	-5N	-2.5N	0N	2.5N	5N	μ
50%	1.05±0.46N	0.80±0.50N	0.43±0.53N	0.57±0.65N	0.57±0.68N	0.68±0.24N
60%	1.39±0.49N	0.78±0.44N	0.41±0.52N	0.56±0.45N	0.60±0.51N	0.75±0.38N
70%	1.45±0.44N	0.96±0.42N	0.35±0.43N	0.73±0.44N	0.82±0.40N	0.86±0.40N
80%	0.87±0.42N	0.40±0.44N	0.37±0.45N	0.43±0.45N	0.36±0.42N	0.49±0.22N

TABLE V
SEE FORCE CONTROL STEADY STATE ERROR FOR DIFFERENT INFLATION LEVELS AND TARGET FORCES IN z-DIRECTION

V_{init} \ $f_{d,z}^{\text{cart}}$	0N	3.75N	7.5N	11.25N	15N	μ
50%	0.59±0.76N	0.72±0.68N	1.10±0.62N	1.54±0.67N	2.10±0.67N	1.21±0.62N
60%	0.56±0.67N	0.66±0.67N	1.02±0.61N	1.32±0.68N	1.64±0.67N	1.04±0.45N
70%	0.48±0.63N	0.65±0.60N	0.91±0.62N	1.24±0.66N	1.54±0.65N	0.96±0.43N
80%	0.49±0.65N	0.65±0.65N	0.82±0.62N	1.00±0.62N	1.11±0.66N	0.82±0.25N

Time series of the step responses are shown in Fig. 12 and the resulting steady-state errors are summarized in Table II as follows.

The controller achieves the desired forces well with a mean absolute steady-state error of 0.47±0.24 N across all configurations and force levels. This is in range with the previously validated quasi-static force sensing accuracy. The precision of the controller remains consistent over all tested configurations. Best results are achieved for demand forces of 4 N and inflations of 70% and 80%. For most test conditions a small, time-dependent change in the steady-state error is observable. The contact force increases over time, whereas the estimated force remains constant. This could be caused by the stress relaxation of the elastic material. Stress relaxation leads to a slow decrease in the internal stress, which in return results in a decreasing estimate of the external force. The controller compensates the falsely measured force difference, resulting in an increasingly higher external force.

D. SEE Force Control

Prior to evaluating the force controller performance, a calibration is undertaken to determine $\boldsymbol{K}_V$. A typical estimate $\hat{\boldsymbol{K}}_V$ is shown as follows.

$$\hat{\boldsymbol{K}}_V = \begin{bmatrix} 43.31 & 1.94 & 1.48 \\ 0.94 & 48.64 & 1.39 \\ 0.36 & 1.18 & 44.18 \end{bmatrix} \text{ with } [\hat{\boldsymbol{K}}_V] = \frac{\text{kPa}}{\text{ml}}. \quad (19)$$

The force controller is implemented as a *PI* controller with gains $G_P = 1.97 \frac{\text{ml}}{\text{s·N}}$ and $G_I = 0.02 \frac{\text{ml·s}}{\text{s·N}}$ The step responses of the combined SEE for different inflation levels and demand forces are evaluated. Steps are given for forces in x-, y-, and z-direction.

The responses are shown in Fig. 13 and steady-state errors are summarized in Tables III– V for measured forces f_x, f_y, and f_z.

The measured force responses show good controllability of the tip force. Larger steady-state force deviations occur only for demanded forces with greater magnitudes of $|f_d| \geq 2.5$ N for x- and y- and $f_d \geq 10$N for z-direction. Across all directions and demanded forces it can be seen that force error decreases significantly with the initial inflation of the SEE. While for 50% inflation the mean steady-state error is 0.98 N, it decreases by 29% to 0.7 N at 80% inflation. The error scales with the magnitude of the force. Similar diverging behavior as seen in the SFA step responses in steady state is mainly observable for large demand forces. Its impact on the controller is significantly lower compared to the controller performance for a single SFA.

E. SEE Force Control–Trajectory Tracking

The controller's ability to track time-varying force demands is validated across six trajectories of which three are executed from

This article has been accepted for inclusion in a future issue of this journal. Content is final as presented, with the exception of pagination.

LINDENROTH et al.: TOWARD INTRINSIC FORCE SENSING AND CONTROL IN PARALLEL SOFT ROBOTS
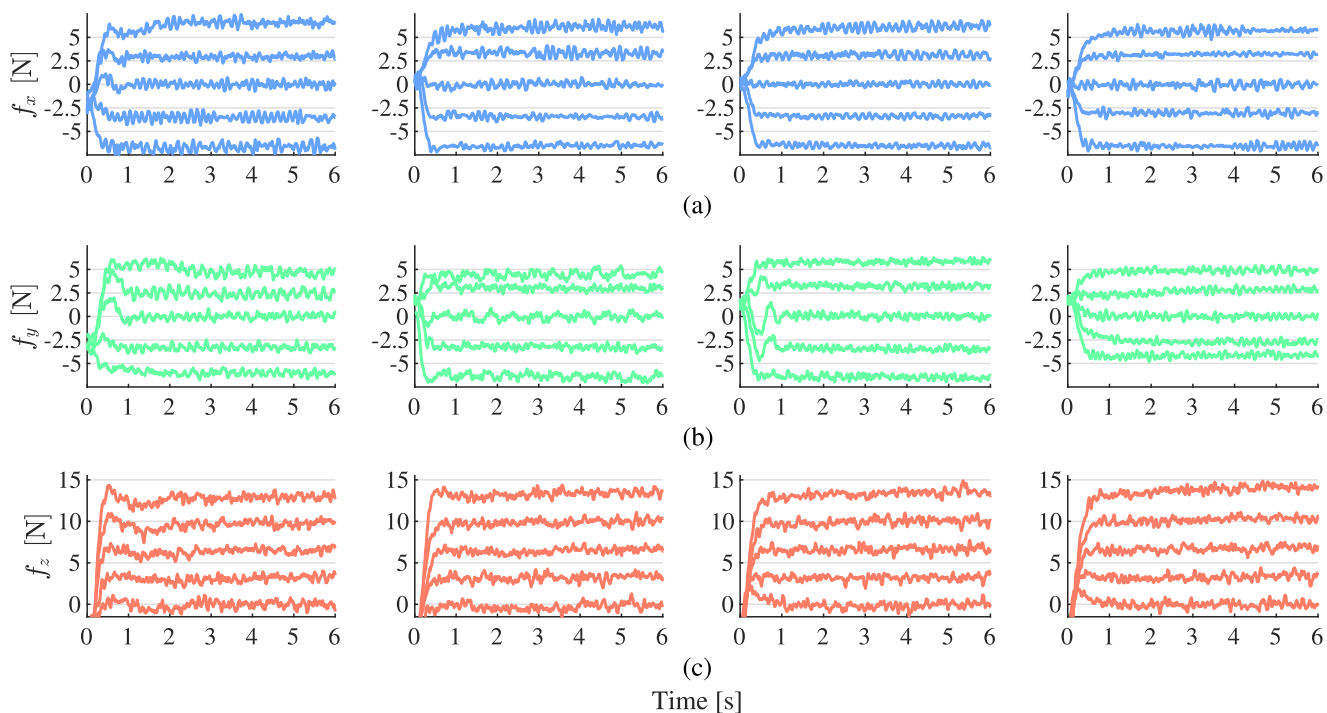9

Fig. 13. Results for SEE step responses at 50%, 60%, 70%, and 80% initial inflation indicating the measured forces for varying demanded forces of -5 N, -2.5 N, 0 N, 2.5, and 5 N in x- (a) and y-axis (b) as well as 0 N, 5 N, 10 N, and 15 N in z-axis (c).

a straight initial configuration and three from deformed initial configurations. In this configuration, the SEE is equipped with SFAs made of Ecoflex 00-45 silicone rubber (Smooth-On Inc., Pennsylvania, USA) and force data are obtained using a Mini40 force–torque sensor. Results are presented in Fig. 14 for six trajectories acquired in six different configurations of the SEE, of which three are in a straight, inflated and three in a deformed configuration. It can be seen that the controller tracks the demanded forces well according to the estimated force feedback. Along the z-direction, estimated and measured forces align well, with slightly larger errors being evident for the passively deformed configurations. Estimation in x-direction appears more accurate when forces are acting in multiple directions, with errors in y being greater. In deformed configurations, both estimation errors in x- and y-direction increase drastically while the estimation in z-direction is still accurate.

IV. DISCUSSION

This article establishes a practical approach to intrinsic force sensing and subsequent force control in fluid-driven soft robotic systems. From the mechanical characterization of the system, it can be seen that a wide range of physical phenomena have to be taken into account to produce a viable model of the system across its entire workspace. This includes a nonconstant, nonlinear force transmission, history-dependent phenomena, which induce pressure and consequently force uncertainty and dynamic effects such as damping. In this work, we determine a range of SFA inflation that allows for simplification and linearization of

these phenomena. It can be seen that these metrics become more consistent upon inducing initial strain in the material.

We have confirmed that it is possible to sense and control external contact forces when the induced working fluid volume and pressure are known. Repeated online calibration of the system is necessary to capture adverse effects such as air bubble formation within the fluid-lines after the initial characterization of the system. Consistent force sensing is then possible across the previously defined range.

It has been shown that intrinsic force sensing in a quasi-static configuration is possible with an average force sensing error of 0.56 ± 0.66 N across varying loads and inflation levels. As shown, various factors contribute to the deterioration of the force sensing accuracy. Hysteresis for example causes history-dependent deviations from the linearized volume–pressure relationship. As the hysteretic behavior of the system is not modeled, this can lead to errors in the prediction of the internal pressure.

A time-dependent deterioration of the steady-state response of both the SFA and SEE force controllers is observable. One factor which greatly contributes to a time-dependent pressure change in an SFA is the relaxation of the utilized elastic silicone rubber material. In some of the SFA and SEE step responses a slow divergence from the demanded force value is noticeable. The relaxation of the material leads to a slow decrease of measured internal pressure in the system. This, in return, leads to an increasing difference between estimated and true force values, resulting in the controller slowly increasing the contact force. To overcome this limitation, relaxation would have to be accounted for in the SFA modeling.
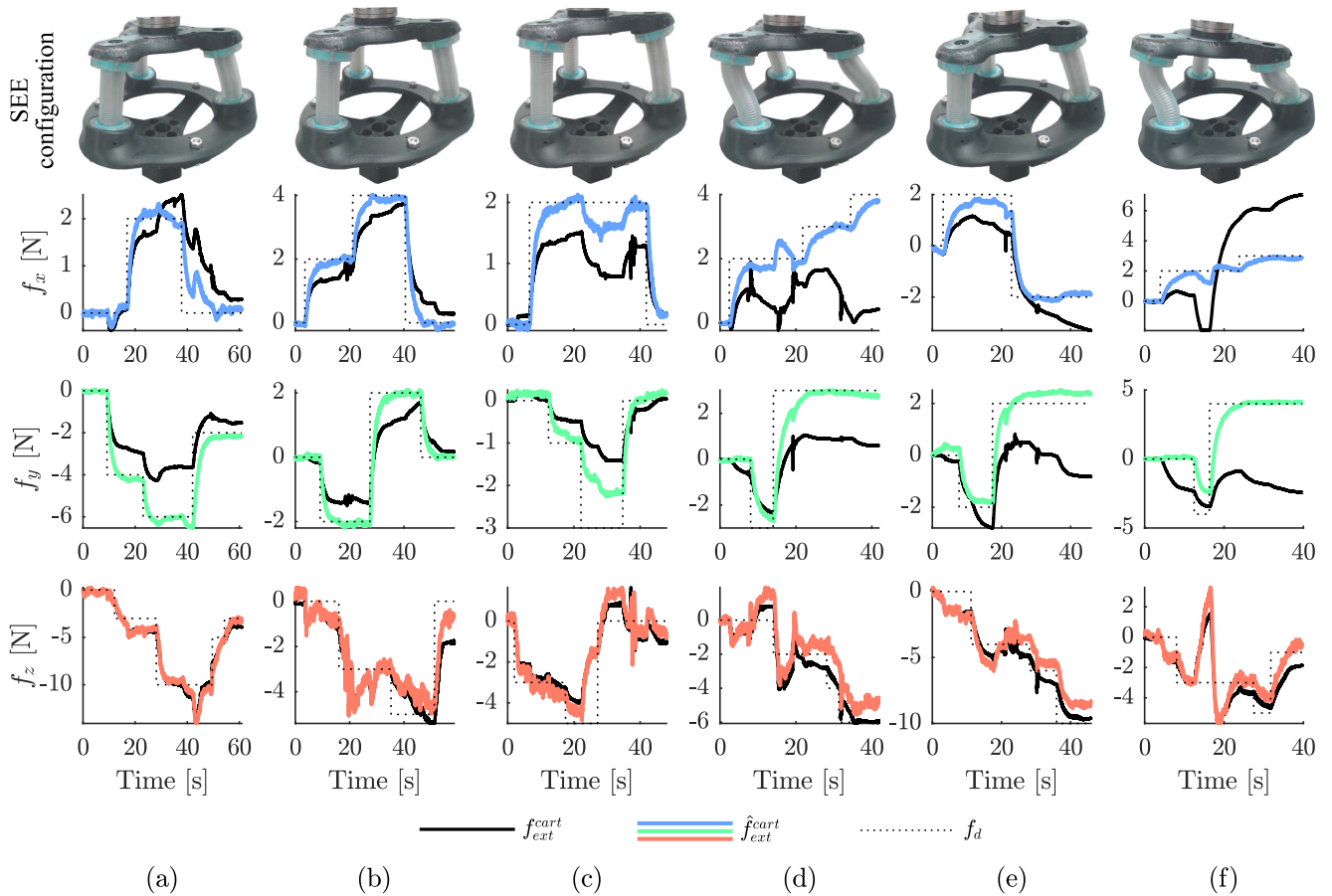
Fig. 14. Time-varying force levels for six trajectories, with the SEE being in straight, inflated (a-c) and in passively deformed configurations (d-f) with measured $f_{\text{ext}}^{\text{cart}}$ and estimated forces $\hat{f}_{\text{ext}}^{\text{cart}}$ in x-, y-, and z-direction.

The previously described linearization of the SFA pressure–volume relationship is another source of error. While it can be seen that deviations from a linear trend are small for the investigated subset of the inflation range, the mean error associated is 0.06 N. Additionally, the assumption of constant force transmissibility for said workspace subset induces errors of approximately 6.69%.

While a number of sources for the occurring errors are identified and discussed, further investigations have to be carried out to determine unmodeled phenomena leading to the reduction in force sensing accuracy. In addition to the investigated sources for errors, the derived mapping from actuator to Cartesian space could lead to inaccuracies when the soft robot is in a deflected configuration. When the linear SFA undergoes deformation, the angle of force application to the moving platform of the robot changes, which could be a possible reason for larger errors occurring when large forces are applied to the soft robot. Determining the force sensing error behavior under large deflections and modeling the respective deformation of the system could thus improve the intrinsic force sensing capabilities.

Moreover, large forces applied axially along the SFAs could lead to compression, which is ignored in the model. This compression under the kinematic constraint of the incompressible fluid volume might result in an expansion of the internal fluid channel, which in return impacts the force transmission and thus lowers the accuracy of the force estimation.

Despite the at times large deviations between measured and estimated forces, the derived force controller is able to track applied contact forces, particularly when the applied force acts primarily along the main axis of the parallel SFAs.

Particularly in the context of robot-assisted ultrasound scanning, which is one of the application focuses of the here-described system, force control is important for delivering a stable image under external disturbances, such as patient motion [25]. While force control in robotics is an established field and systems commonly achieve higher accuracy and controllability of the contact force than our proposed solution, both in the context of traditional rigid robotics systems [26] as well as soft robotics [27], [28], they commonly rely on dedicated sensors. To the best of our knowledge, no soft, fluid-actuated intrinsic force control approach has been derived. Placing fluid pressure sensors away from the end-effector can have profound advantages in achieving low-cost, highly integrated and potentially MRI-compatible force-sensing systems. Our future work will aim at improving accuracy to achieve performances closer to those in dedicated sensors, which will allow for wider adoption and greater generalizability of the approach. For the application of soft robot-guided ultrasound scanning, the accuracy of our

intrinsic force controller appears to be as high as that of human operators during manual ultrasound scanning, thus potentially rendering our system a viable solution [29].

V. CONCLUSION

This article derived approaches to intrinsic force sensing and control for fluid-driven soft robots. This is achieved incrementally from static sensing, which had first been shown in our previous work. An investigation into the mechanical characteristics of SFAs is provided and limitations in force sensing are identified. It has been found that for a single actuator the external force can be sensed with an accuracy of 0.56 ± 0.66 N in a quasi-static configuration. The intrinsic force sensing approach has been applied in a closed-loop force controller for a single SFA. For static contacts, the force can be controlled with a steady-state accuracy of 0.47 ± 0.24 N. The controller has been expanded to the SEE, which is comprised of three SFAs arranged in a parallel, angled configuration. With this setup, it has been shown that forces can be controlled along all three Cartesian axes.

REFERENCES

[1] M. Runciman, A. Darzi, and G. P. Mylonas, "Soft robotics in minimally invasive surgery," *Soft Robot.*, vol. 6, no. 4, pp. 423–443, 2019.

[2] J. Back et al., "Three dimensional force estimation for steerable catheters through bi-point tracking," *Sensors Actuators, A: Phys.*, 2018, pp. 404–415.

[3] K. C. Galloway et al., "Soft robotic grippers for biological sampling on deep reefs," *Soft Robot.*, vol. 3, no. 1, pp. 23–33, 2016.

[4] L. Lindenroth et al., "Design of a soft, parallel end-effector applied to robot-guided ultrasound interventions," in *Proc. IEEE Int. Conf. Intell. Robots Syst.*, 2017, pp. 3716–3721.

[5] L. Lindenroth, R. J. Housden, S. Wang, J. Back, K. Rhode, and H. Liu, "Design and integration of a parallel, soft robotic end-effector for extracorporeal ultrasound," *IEEE Trans. Biomed. Eng.*, vol. 67, no. 8, pp. 2215–2229, Aug. 2020.

[6] P. Puangmali, K. Althoefer, L. D. Seneviratne, D. Murphy, and P. Dasgupta, "State-of-the-art in force and tactile sensing for minimally invasive surgery," *IEEE Sensors J.*, vol. 8, no. 4, pp. 371–381, Apr. 2008.

[7] K. S. Hoffmayer and E. P. Gerstenfeld, "Contact force-sensing catheters," *Curr. Opin. Cardiol.*, vol. 30, no. 1, pp. 74–80, 2015.

[8] P. Polygerinos, L. D. Seneviratne, R. Razavi, T. Schaeffter, and K. Althoefer, "Triaxial catheter-tip force sensor for MRI-guided cardiac procedures," *IEEE/ASME Trans. Mechatronics*, vol. 18, no. 1, pp. 386–396, Feb. 2013.

[9] A. Rostami et al. "Microsphere and fiber optics based optical sensors," *Opt. Sensors-New Dev. Pract. Appl*, 2014.

[10] H. Xie, H. Liu, Y. Noh, J. Li, S. Wang, and K. Althoefer, "A fiber-optics-based body contact sensor for a flexible manipulator," *IEEE Sensors J.*, vol. 15, no. 6, pp. 3543–3550, Jun. 2015.

[11] A. Shiva et al., "Elasticity versus hyperelasticity considerations in quasistatic modeling of a soft finger-like robotic appendage for real-time position and force estimation," *Soft Robot.*, vol. 6, no. 2, pp. 228–249, 2019.

[12] L. Seminara et al., "Piezoelectric polymer transducer arrays for flexible tactile sensors," *IEEE Sensors J.*, vol. 13, no. 10, pp. 4022–4029, Oct. 2013.

[13] J. B. Chossat, Y. L. Park, R. J. Wood, and V. Duchaine, "A soft strain sensor based on ionic and metal liquids," *IEEE Sensors J.*, vol. 13, no. 9, pp. 3405–3414, Sep. 2013.

[14] R. K. Kramer, "Soft electronics for soft robotics," *Micro- Nanotechnol. Sens. Syst. Appl. VII*, vol. 9467, 2015, Art. no. 946707.

[15] M. Khoshnam, A. C. Skanes, and R. V. Patel, "Modeling and estimation of tip contact force for steerable ablation catheters," *IEEE Trans. Biomed. Eng.*, vol. 62, no. 5, pp. 1404–1415, May 2015.

[16] D. C. Rucker and R. J. Webster, "Deflection-based force sensing for continuum robots: A probabilistic approach," in *Proc. IEEE Int. Conf. Intell. Robots Syst.*, 2011, pp. 3764–3769.

[17] H. Yuan, P. W. Y. Chiu, and Z. Li, "Shape-reconstruction-Based force sensing method for continuum surgical robots with large deformation," *IEEE Robot. Automat. Lett.*, vol. 2, no. 4, pp. 1972–1979, Oct. 2017.

[18] Z. Zhang, J. Dequidt, and C. Duriez, "Vision-based sensing of external forces acting on soft robots using finite element method," *IEEE Robot. Automat. Lett.*, vol. 3, no. 3, pp. 1529–1536, Jul. 2018.

[19] J. Back, L. Lindenroth, R. Karim, K. Althoefer, K. Rhode, and H. Liu, "New kinematic multi-section model for catheter contact force estimation and steering," in *Proc. IEEE Int. Conf. Intell. Robots Syst.*, 2016, pp. 2122–2127.

[20] K. Xu and N. Simaan, "An investigation of the intrinsic force sensing capabilities of continuum robots," *IEEE Trans. Robot.*, vol. 24, no. 3, pp. 576–587, Jun. 2008.

[21] K. Xu and N. Simaan, "Intrinsic wrench estimation and its performance index for multisegment continuum robots," *IEEE Trans. Robot.*, vol. 26, no. 3, pp. 555–561, Jun. 2010.

[22] D. Haraguchi, K. Tadano, and K. Kawashima, "A prototype of pneumatically-driven forceps manipulator with force sensing capability using a simple flexible joint," in *Proc. IEEE Int. Conf. Intell. Robots Syst.*, 2011, pp. 931–936.

[23] C. B. Black, J. Till, and D. C. Rucker, "Parallel continuum robots: Modeling, analysis, and actuation-based force sensing," *IEEE Trans. Robot.*, vol. 34, no. 1, pp. 29–47, Feb. 2018.

[24] L. Lindenroth, C. Duriez, J. Back, K. Rhode, and H. Liu, "Intrinsic force sensing capabilities in compliant robots comprising hydraulic actuation," in *Proc. IEEE Int. Conf. Intell. Robots Syst.*, 2017, pp. 2923–2928.

[25] S. E. Salcudean, H. Moradi, D. G. Black, and N. Navab, "Robot-assisted medical imaging: A review," *Proc. IEEE Proc. IRE*, vol. 110, no. 7, pp. 951–967, 2022.

[26] K. Mathiassen, J. E. Fjellin, K. Glette, P. K. Hol, and O. J. Elle, "An ultrasound robotic system using the commercial robot UR5," *Front. Robot. AI*, vol. 3, pp. 1–16, 2016.

[27] P. Abbasi, M. A. Nekoui, M. Zareinejad, P. Abbasi, and Z. Azhang, "Position and force control of a soft pneumatic actuator," *Soft Robot.*, vol. 7, no. 5, pp. 550–563, 2020.

[28] H. Wang, H. Ni, J. Wang, and W. Chen, "Hybrid vision/force control of soft robot based on a deformation model," *IEEE Trans. Control Syst. Technol.*, vol. 29, no. 2, pp. 661–671, Mar. 2021.

[29] M. W. Gilbertson and B. W. Anthony, "Force and position control system for freehand ultrasound," *IEEE Trans. Robot.*, vol. 31, no. 4, pp. 835–849, Aug. 2015.

Lukas Lindenroth (Member, IEEE) received the Ph.D. degree in robotics from King's College London (KCL), London, U.K., in 2020, where he developed soft robotic solutions for diagnostic ultrasound.

He is currently a Lecturer in surgical robotics with the Department of Surgical and Interventional Engineering within the School of Biomedical Engineering and Imaging Sciences, King's College London, London, U.K. His research focuses on using novel robotics technologies such as soft robotics to develop medical devices for improved patient outcomes and clinician experience. Prior to this role, he was Postdoctoral Research Fellow with the Wellcome / EPSRC Centre for Interventional and Surgical Sciences at University College London.

Danail Stoyanov (Senior Member, IEEE) received the Ph.D. degree in computer science from the Imperial College London, London, U.K., in 2006, where he specialized in medical image computing.

He is currently a Professor of robot vision with the Department of Computer Science, University College London, London, U.K., the Director of the Wellcome/EPSRC Centre for Interventional and Surgical Sciences (WEISS), a Royal Academy of Engineering Chair in Emerging Technologies and the Head Scientist at Digital Surgery, Medtronic. He first studied Computer Systems and Electronics at King's College London.

Kawal Rhode received his B.Sc. (hons) degree in radiological sciences and basic medical sciences from King's College London, London, U.K. in 1992, and the Ph.D. degree in medical physics from the University College London, London, U.K., in 2006. He was appointed as a Lecturer in image processing with King's College London, London, U.K., in 2007, a Senior Lecturer, in 2011, a Reader in biomedical engineering, in 2015, and a Professor, in 2016. His current research interests include image-guided interventions, intelligent mechatronics systems for interventions and ultrasound imaging, 3D printing in healthcare and pedagogy for biomedical engineering. He has more than 400 publications in journals, conference proceedings, book chapters, and patents. He is the Head of Education for the School of Biomedical Engineering and Imaging Sciences, where he oversees the School's delivery of taught programmes, including the BEng/MEng Biomedical Engineering, MSc/MRes Healthcare Technologies, and the iBSc Imaging Sciences.

Hongbin Liu is currently a Professor with the Chinese Academy of Sciences, Institute of Automation (CASIA), an Executive Deputy Director for the Centre of AI and Robotics (CAIR), Hong Kong Institute of Science & Innovation, Chinese Academy of Sciences. He is also affiliated with the School of Biomedical Engineering and Imaging Sciences, Faculty of life Sciences and Medicine, King's College London (KCL), where he is directing the Haptic Mechatronics and Medical Robotics Laboratory (HaMMeR). He established the intelligent minimally invasive technologies group at CAISA, focusing on the research and development of robotic systems with advanced haptic perception and interaction capabilities, to enable safer and more effective minimally invasive diagnosis and treatment for patients. The group's long-term vision is to digitize surgery via augmenting multimode sensing capability and intelligence of surgical robotic systems. He has authored or coauthored more than 110 peer-reviewed articles with a H-index 34. His research has been funded by Chinese Academy of Sciences, EPSRC, Innovate U.K., NHS Trust and EU Commissions, with strong industrial collaborations with MedTech industries. His research has led to the clinical translation of a series of flexible robotic endoscopic systems for applications such as colonoscopy, bronchoscopy as well as vascular surgeries.